

Article

# Temperature-Dependent Elastic Properties of B<sub>4</sub>C from First-Principles Calculations and Phonon Modeling

Sara Sheikhi <sup>\*</sup>, Wylie Stroberg  and James D. Hogan 

Department of Mechanical Engineering, University of Alberta, Edmonton, AB T6G 2R3, Canada; stroberg@ualberta.ca (W.S.); jdhogan@ualberta.ca (J.D.H.)

\* Correspondence: ssheikhi@ualberta.ca

**Abstract:** Boron carbide plays a crucial role in various extreme environment applications, including thermal barrier coatings, aerospace applications, and neutron absorbers, because of its high thermal and chemical stability. In this study, the temperature-dependent elastic stiffness constants, thermal expansion coefficient, Helmholtz free energy, entropy, and heat capacity at a constant volume ( $C_v$ ) of rhombohedral B<sub>4</sub>C have been predicted using a quasi-harmonic approach. A combination of volume-dependent first-principles calculations (density functional theory) and first-principles phonon calculations in the supercell framework has been performed. Good agreement between the elastic constants and structural parameters from static calculations is observed. The calculated thermodynamic properties from phonon calculations show trends that align with the literature. As the temperature rises, the predicted free energy follows a decreasing trend, while entropy and  $C_v$  follow increasing trends with temperature. Comparisons between the predicted room temperature thermal expansion coefficient (TEC) ( $7.54 \times 10^{-6} \text{ K}^{-1}$ ) and bulk modulus (228 GPa) from the quasi-harmonic approach and literature results from experiments and models are performed, revealing that the calculated TEC and bulk modulus fall within the established range from the limited set of data from the literature (TEC =  $5.73\text{--}9.50 \times 10^{-6} \text{ K}^{-1}$ , B = 221–246 GPa). Temperature-dependent  $C_{ij}$ s are predicted, enabling stress analysis at elevated temperatures. Overall, the outcomes of this study can be used when performing mechanical and thermal stress analysis (e.g., space shielding applications) and optimizing the design of boron carbide materials for elevated temperature applications.



**Citation:** Sheikhi, S.; Stroberg, W.; Hogan, J.D. Temperature-Dependent Elastic Properties of B<sub>4</sub>C from First-Principles Calculations and Phonon Modeling. *Ceramics* **2024**, *7*, 235–249. <https://doi.org/10.3390/ceramics7010015>

Academic Editors: Jacques Lamon and Gilbert Fantozzi

Received: 14 December 2023

Revised: 12 February 2024

Accepted: 19 February 2024

Published: 21 February 2024



**Copyright:** © 2024 by the authors. Licensee MDPI, Basel, Switzerland. This article is an open access article distributed under the terms and conditions of the Creative Commons Attribution (CC BY) license (<https://creativecommons.org/licenses/by/4.0/>).

**Keywords:** density functional theory; phonon calculations; quasi-harmonic approach; boron carbide; temperature-dependent elastic and thermal properties

## 1. Introduction

Advanced ceramics, such as boron carbide, exhibit low density ( $\sim 2.5 \frac{\text{g}}{\text{cm}^3}$  [1]), high strength ( $\sim 3$  to 5 GPa [2]), high hardness ( $\sim 25$  to 38 GPa [3]), high melting temperature (2723 K [4]), and high chemical and thermal stability [5]. These desirable properties make boron carbide suitable for applications involving extreme environments, including aerospace [6], body armor [7], wear-resistant components [8], abrasive powder [9], and neutron absorbers [10]. Given the significance of advanced ceramics in various industries (e.g., medical devices [11], and aircraft and satellite components [12]) and broad research interests toward understanding their behavior under extreme conditions, accurately predicting their behavior and mechanical properties is crucial for designing and optimizing boron carbide-based materials. Computational methods like molecular dynamics and density functional theory provide efficient tools to investigate the behavior of materials under different loading conditions, with reduced cost and time compared to experimental approaches [13,14]; these tools are used here to study the effects of temperature on the elastic and thermal properties of boron carbide. The primitive cell of boron carbide is a rhombohedral lattice composed of 15 atoms with 12-atom boron icosahedra and a 3-atom chain in the middle of the lattice with the configuration of B<sub>12</sub>C<sub>3</sub> or B<sub>4</sub>C [15]. The covalent

bonds between B and C atoms contribute to the overall thermal and structural stability of the material [9,16].

Traditional methods for predicting the elastic properties of materials rely on empirical relationships, such as Hooke's law, which are based on experimental data and generally provide reasonable estimates for well-established materials [17]. However, these methods can be limited when applied to extreme conditions (e.g., very low or high temperatures [18], high pressure [19], and corrosive environments [20]), as well as for complex materials (e.g., advanced ceramics [21,22] and composites [23,24]). The elastic properties reported for boron carbide typically originate from room-temperature experimental setups. For example, the Young's modulus of B<sub>4</sub>C, measured using acoustic methods, falls within the range of 460–470 GPa [25,26]. Several studies have predicted the bulk modulus of boron carbide at room temperature through experiments [27] and atomistic calculations [28]. These studies suggest a range of 220–250 GPa for the bulk modulus of B<sub>4</sub>C at 298 K. Although the elastic properties of boron carbide have been extensively studied at room temperature [27–32], there is still a gap in the knowledge regarding how these properties vary at elevated temperatures, where boron carbide has numerous applications. Challenges arise from the need for extensive experimental testing and the difficulty of capturing the full complexity of material behavior. Traditional methods often overlook factors like microstructural effects [23], anisotropy [33], and temperature dependence [34]. To address these challenges, advanced computational techniques, including first-principles methods [28,35,36], molecular dynamics simulations [21,37], and machine learning approaches [14,38], have been developed. These methods not only enable more accurate predictions of elastic properties, but also, when appropriately validated, can overcome the limitations of traditional approaches based solely on empirical relationships and experimental data [17,39]. Significant advancements in computer resources and first-principles methodologies have enabled the prediction of single crystal static elastic stiffness constants ( $C_{ij}$ s) at 0 K using the strain energy and stress–strain methods. As an example, the elastic constants of single crystal materials such as B<sub>4</sub>C [28], Al<sub>2</sub>O<sub>3</sub> [40], Ti<sub>3</sub>B<sub>4</sub> [41], and Fe<sub>3</sub>C [42] have been successfully predicted through first-principles calculations. In addition to this, density functional theory and molecular dynamics simulations have been used for investigating the microstructure and mechanical properties [43], phase transformation and amorphization [44], and semiconductor behavior of boron carbide [45]. Despite these achievements, the exploration of the pressure dependence of elastic constants has received more attention, while the estimation of  $C_{ij}$ s at elevated temperatures remains largely unexplored, except for molecular dynamics simulations, which can lack sufficient accuracy at different temperatures [34,46]. While MD simulations offer a detailed understanding of dynamic behavior, their computational intensity and the accuracy of interatomic potentials may limit their feasibility for extensive exploration of high-temperature regimes, especially in the context of single crystal calculations for materials like boron carbide [34,39,46]. To address this gap, this article focuses on the calculation of the temperature-dependent elastic properties of single crystal B<sub>4</sub>C boron carbide, through the use of a quasi-harmonic approach involving density functional theory (DFT) and phonon calculations. Since first-principles methods typically provide calculations at zero temperature, the quasi-harmonic approach [47] is employed to obtain temperature-dependent elastic properties. The quasi-harmonic approach incorporates the effects of temperature by considering the Helmholtz free energy, which has thermal electronic and vibrational contributions to the material's properties [35,47]. This allows for a more comprehensive understanding of the temperature-dependent elastic behavior of boron carbide. This approach has been previously applied to other materials such as alumina (Al<sub>2</sub>O<sub>3</sub>) [34], nickel aluminide (Ni<sub>3</sub>Al) [35], and lead titanate (PbTiO<sub>3</sub>) [47].

In the present work, we organize the article as follows. In Section 2, we present the theory and methodology employed to find the temperature-dependent elastic constants, including the Helmholtz free energy, static calculations and equation of state (EOS) for total energy versus cell volume (E-V) results, vibrational contributions based on phonon calculations, and the details of our first-principles calculations. In Section 3, the details of

the DFT model validation, the properties calculated from the EOS, and the results of phonon calculations are provided. Results are discussed in the context of comparing structural parameters and elastic properties with literature data, static calculations and the equation of state, phonon calculations, temperature-dependent thermal and elastic properties, and the thermal expansion coefficient. The limitations of the current work are also provided in this section. In Section 4, conclusions of the present work are given.

## 2. Theory and Methodology

Density functional theory provides calculations at zero temperature [48]. To obtain the temperature-dependent elastic properties in this study, a quasi-harmonic approach [49] within the Helmholtz free energy framework is applied. The quasi-harmonic approach accurately captures temperature-dependent lattice variations, allowing a comprehensive analysis of the material's elastic behavior across a wider temperature range [47,49–51].

The Helmholtz free energy  $F(V, T)$  at volume  $V$  and temperature  $T$  is approximated by

$$F(V, T) = E(V) + F_{vib}(V, T) + F_{ele}(V, T), \quad (1)$$

where  $E(V)$  is the static energy at 0 K and volume  $V$  determined by DFT calculations. The vibrational contribution to the free energy at volume  $V$  and temperature  $T$  is defined by  $F_{vib}(V, T)$ , estimated by first-principles phonon calculations. The thermal electronic contribution to free energy is represented by  $F_{ele}(V, T)$ , which is zero in the case of semiconductors and insulators due to the absence of electrons at the Fermi level [34,35,52]. Given that boron carbide exhibits semiconductor behavior [53], the  $F_{ele}(V, T)$  term is disregarded in this study. In the following, the details of the equations and methods for static energy calculation (Section 2.1), vibrational contribution to the Helmholtz free energy (Section 2.2), and DFT and phonon calculations (Section 2.3) are provided.

### 2.1. Static Energy and E-V Equation of State

Various equations of state (EOS) for E-V relationships have been established in the literature. The most widely used EOS is the Birch–Murnaghan EOS (BM) [54]. The 4-parameter equation of the Birch–Murnaghan EOS has the following form:

$$E(V) = a + bV^{-n/3} + cV^{-2n/3} + dV^{-3n/3}, \quad (2)$$

where  $a$ ,  $b$ ,  $c$ , and  $d$  are the fitting parameters. In this study, we have adopted the modified Birch–Murnaghan (mBM) EOS proposed by Teter et al. [55], for which  $n = 1$ , to fit the E-V data of  $B_4C$ , due to its ability to minimize fitting errors [35].

The bulk modulus corresponding to the mBM EOS is

$$B_e = \frac{2(9d + 5cV_e^{1/3} + 2bV_e^{2/3})}{9V_e^2}, \quad (3)$$

where  $V_e$  is the equilibrium volume. According to the first-principles methods of EOS fitting, a single-phase region with a volume range of approximately  $\pm 10\%$  around the equilibrium volume should be considered. Additionally, it is recommended to use a minimum of five data points for EOS fitting [35].

### 2.2. Vibrational Contribution to the Helmholtz Free Energy

The vibrational contribution to the Helmholtz free energy as a function of volume ( $V$ ) and temperature ( $T$ ) is

$$F_{vib}(V, T) = k_B T \int_0^\infty \ln \left[ 2 \sinh \frac{\hbar \omega}{2k_B T} \right] g(\omega) d\omega, \quad (4)$$

where  $k_B$  is the Boltzmann constant,  $\hbar$  is the reduced Planck constant,  $\omega$  is the frequency, and  $g(\omega)$  is the phonon density of states (DOS). To obtain the vibrational contribution to the Helmholtz free energy, a systematic approach is undertaken. After finding the ground

state properties of the initial structures from DFT calculations, the supercell method [56] is used to calculate the phonon dispersion relations. These relations describe the vibrational frequencies as a function of wave vector in the Brillouin zone. The force constants, which quantify how the potential energy changes with atomic displacement are then obtained from the DFT results. By analyzing the force-sets and phonon dispersion relations [56], the phonon DOS is calculated, which gives information about the distribution of vibrational frequencies. Utilizing force-sets and DOS and statistical mechanics, the thermodynamic properties are calculated as a function of temperature [56]. By repeating this process for different volumes of the initial structure, the thermodynamic properties are obtained as a function of temperature and volume. Then the T-V relationship is obtained by minimizing the  $F(V)$  for each temperature.

### 2.3. DFT and Phonon Calculations

DFT calculations were performed using the Vienna ab initio simulation package (VASP) [57,58]. The Projector Augmented Wave with Perdew–Burke–Ernzerhof (PAW-PBE) pseudopotential [59] with a cut-off energy of 520 eV for plane waves was employed. The PAW-PBE has been widely used in the literature within DFT simulations for electronic structure calculations because of its high accuracy and reliability [59]. For k-point sampling, the Gamma scheme with fine accuracy ( $11 \times 11 \times 11$  k-mesh for the unit cell with equilibrium volume as shown in Figure 1a) was used, with a careful assessment of k-point convergence to ensure reliable results. Next, the integration of band structure energy across the Brillouin zone was accomplished using the tetrahedron method with Blöch corrections [60]. This method effectively accounts for the total energy, ion forces, and stresses in semiconductors and insulators (e.g., Si [61],  $\text{Al}_2\text{O}_3$  [35], and  $\text{SiO}_2$  [62]), and is also suitable for simulating the current structure because boron carbide exhibits semiconductor properties [63,64]. The Generalized Gradient Approximation (GGA) [65] was used for the exchange–correlation functional. During the structural optimization, the ionic relaxation scheme with a conjugate gradient algorithm was employed. Additionally, the relaxation of both the cell shape and atomic positions throughout the optimization process was ensured. The incorporation of these two parameters ensures a more precise representation of the equilibrium structure of the system [66]. The VASPkit code [67] was used for k-point generation and post-processing of the VASP calculated data.

Phonon calculations within the supercell framework [56] with supercells of  $3 \times 3 \times 1$  cells and 135 atoms as shown in Figure 1b were employed to determine the vibrational contribution to the Helmholtz free energy (Equation (1)). The acting forces on atoms for each supercell of  $\text{B}_4\text{C}$  were calculated with DFT by VASP (v.5.4.4) with a  $4 \times 4 \times 11$  k-mesh. Phonopy software (v.2.19.1), a package for phonon calculations at harmonic and quasi-harmonic levels [68], was used for frozen phonon calculations and post-processing of the results. The supercell sizes of  $3 \times 3 \times 1$  and  $3 \times 3 \times 3$  were studied in phonon calculations. The phonon calculation results and thermal properties for both cells matched and the  $3 \times 3 \times 1$  size was chosen as the supercell size to reduce the computational expenses. The studied structures in this study are perfect crystal boron carbides and they do not have any defects. Seven different  $\text{B}_4\text{C}$  cells with varying cell volumes were considered to find the relationship between  $V$  and  $T$ . Phonon dispersion curves are obtained from the self-consistent field calculations of the supercells by DFT. The force constants for each volume are calculated from the force-sets derived from self-consistent field (SCF) calculations by DFT. Phonon DOSs are then calculated for each of the volumes from force constants and principles of statistical mechanics [56] resulting in temperature-dependent properties of boron carbide. The crystal structures and visualizations presented in this study were generated using VESTA software (v.3.5.7) [69].

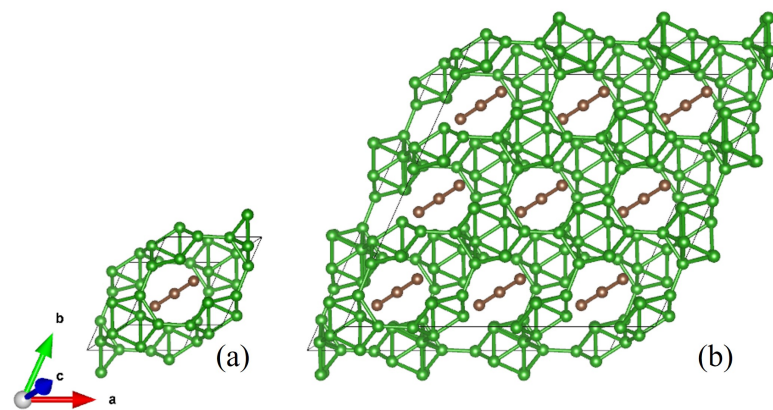


**Figure 1.** Atomistic visualization (by VESTA software (v.3.5.7) [69]) of the rhombohedral boron carbide (a) unit cell with an arrangement of  $B_4C$  and (b) supercell with the same atomic configuration.

In the following, the validation of the DFT model and outcomes of static and phonon calculations including the temperature-dependent thermal and elastic properties are presented and discussed.

### 3. Results and Discussion

In this section, the DFT calculations are validated (Section 3.1). Then, we present studies of the EOS and static energy contribution (Section 3.2), along with the vibrational contribution (Section 3.3) to the Helmholtz free energy for  $B_4C$ . Using the properties derived from the static calculations and insights obtained from phonon calculations, we provide the temperature-dependent thermal and elastic properties of  $B_4C$ .

#### 3.1. First-Principles Calculations' Validation

To validate our DFT calculations for boron carbide, we compared the relaxed lattice parameters, cell volume, energy per atom, and elastic parameters with experimental [29,30,70,71] and modeling [28,72–74] literature data.

Table 1 presents a detailed comparison of the lattice constants, cell volume, and total energy per atom for  $B_4C$  obtained from different literature sources. This agreement (less than 2% relative error) indicates the robustness of our computational approach in accurately predicting the atomic structure of  $B_4C$ . Tables 2 and 3 show the calculated elastic constants and properties for  $B_4C$  with DFT in this work and previous works. By comparing the DFT-calculated elastic properties with data available in the literature and from experimental measurements, a comprehensive assessment of the accuracy and reliability of the DFT results can be achieved. Understanding elastic properties, including Young's modulus ( $E$ ), shear modulus ( $G$ ), bulk modulus ( $B$ ), and Poisson's ratio ( $\nu$ ), is crucial for unraveling the behavior of materials, guiding predictions of failure mechanisms [33,75], understanding dynamic loading in ceramics [21,37], and recognizing temperature dependency [26,34] under extreme conditions.

Figure 2 illustrates the DFT total energies calculated for  $B_4C$  at various volumes (including the equilibrium volume), alongside the fitted E-V mBM EOS curve. The volumes were adjusted through uniform deformation applied to each direction while maintaining a consistent rhombohedral lattice shape, as is suggested in the literature [34,76]. This approach facilitates the comparison of independent elastic constants, ensuring uniformity across different structures. The fitting demonstrates the effectiveness of the chosen EOS in representing the material's behavior across different volumes.

**Table 1.** Comparison of the relaxed lattice parameters, cell volume, and total energy of B<sub>4</sub>C in the rhombohedral system.

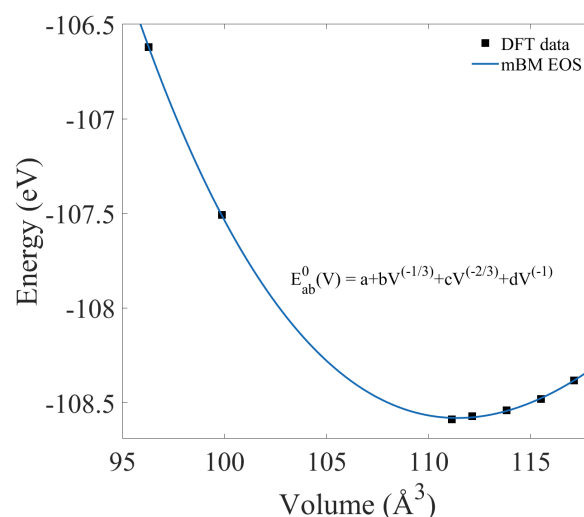
	$a, b, c$ (Å)	$\alpha, \beta, \gamma$	Cell Volume (Å <sup>3</sup> )	Energy per Atom (eV/atom)
Calculation				
Present work	5.185	65.89	111.12	−7.239
Taylor et al. (2012) [28]	5.190	66.01	112.09	
Materials Project [74]	5.180	65.95	110.65	
Dekura et al. (2010) [72]	5.110	66.00		−7.231
Bylander et al. (1990) [73]	5.182	65.61		
Experiment				
Kwei et al. (1996) [70]	5.155	65.67		
McClellan et al. (2001) [71]	5.190	65.18		

**Table 2.** Comparison of the elastic constants of B<sub>4</sub>C in the rhombohedral system.

$C_{ij}$ (GPa)	$C_{11}$	$C_{12}$	$C_{13}$	$C_{14}$	$C_{33}$	$C_{44}$
Present work	465	125	103	36	498	175
Taylor et al. (2012) [28]	486	188	64	14	518	133

**Table 3.** Comparison of the elastic properties of B<sub>4</sub>C in the rhombohedral system.

Elastic Properties	$E$ (GPa)	$G$ (GPa)	$B$ (GPa)	$\nu$
Calculation				
Present work	421	177	225	0.19
Taylor et al. (2012) [28]	451	173	221	
Experiment				
Manghnani et al. (2000) [29]	462	197	235	0.17
Gieske et al. (1991) [30]	472	200	247	0.18

**Figure 2.** DFT energy versus volume of the cell for boron carbide and the fitted mBM EOS.

The fitted EOS is also validated through a comparison of the bulk modulus. The bulk modulus calculated from Equation (3) is compared with the results of DFT for the equilibrium cell of B<sub>4</sub>C, other calculations [28,31,32], and experiments [27,29,30]. Table 4 presents a validation of the bulk modulus for single crystal B<sub>4</sub>C. The comparison between the bulk modulus values obtained from the fitted EOS, our DFT calculations, experimental data [27,29,30], and other calculations [28,31,32] confirms the accuracy and reliability

of our computational approach. The bulk modulus of B<sub>4</sub>C computed from mBM EOS (239 GPa) and DFT (225 GPa) both fall into the range of 220–246 GPa that was established for B<sub>4</sub>C [28–30].

**Table 4.** Validation of bulk modulus calculated from fitted EOS and DFT for single crystal B<sub>4</sub>C.

Method	Bulk Modulus (GPa)
B EOS (Equation (3))	239
Present work (DFT)	225
Experiment	235 [29], 247 [30], 240 [27]
Calculation	234 [31], 246 [29], 221 [28], 239 [32]

### 3.2. Properties from Static Calculations

In addition to the total energy, the elastic stiffness constants of B<sub>4</sub>C were calculated with DFT simulations for seven different cell volumes. In this study, the DFT calculations provided valuable insights into these elastic properties. Figure 3 shows the six independent elastic constants of the single crystal B<sub>4</sub>C structures from DFT simulation for each volume (shown as square data points). The volume-dependent C<sub>ij</sub>s are fitted by exponential functions, which will be used in combination with phonon calculation results to predict temperature-dependent C<sub>ij</sub>s. The circle data points represent the data from previous DFT calculations performed by Taylor et al. [28] showing elastic constants at the equilibrium volume of a B<sub>4</sub>C unit cell. The small difference between these results arises from variations in structural relaxation (as shown in Table 1) and elastic constant calculation processes. The elastic constant versus volume curves for boron carbide exhibit dissimilar trends, reflecting its complex anisotropic behavior. Specifically, C<sub>11</sub>, C<sub>12</sub>, C<sub>13</sub>, C<sub>14</sub>, and C<sub>33</sub> show decreasing trends as the volume increases, indicating a weakening stiffness and reduced resistance to elongation along specific crystallographic directions. This behavior can be attributed to structural softening, lattice expansion, and anisotropic bonding [9]. In contrast, C<sub>44</sub> demonstrates an increasing trend, suggesting a higher resistance to shear deformation along certain crystallographic planes as the volume expands. These findings highlight the complexity of boron carbide’s mechanical response, which is a consequence of its unique crystal structure and the arrangement of boron and carbon atoms within the lattice [9,28].

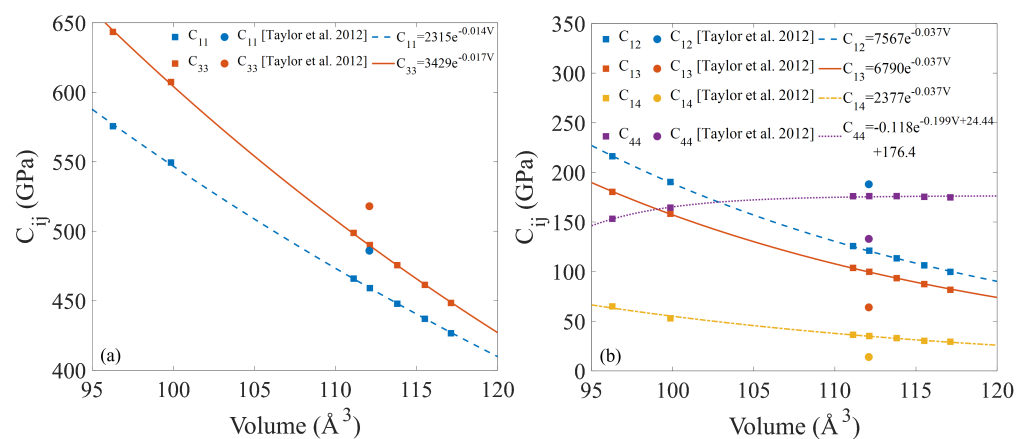


**Figure 3.** Calculated independent elastic constants (a) C<sub>11</sub> and C<sub>33</sub> and (b) C<sub>12</sub>, C<sub>13</sub>, C<sub>14</sub>, and C<sub>44</sub> for single crystal boron carbide using DFT and their trend with cell volume change alongside with literature data for equilibrium volume [28].

### 3.3. Phonon Calculation and Thermal Properties

Combining the E-V results from static calculations at different volumes (Figure 2) with temperature-dependent thermal properties from phonon calculations (provided in Supplementary Materials) results in free energy vs. volume curves for different tempera-

tures and establishes the relationship between volume and temperature (V-T), as shown in Figure 4b. Specifically, Figure 4a depicts the free energy as a function of volume for different temperatures starting from 0 to 1900 K.

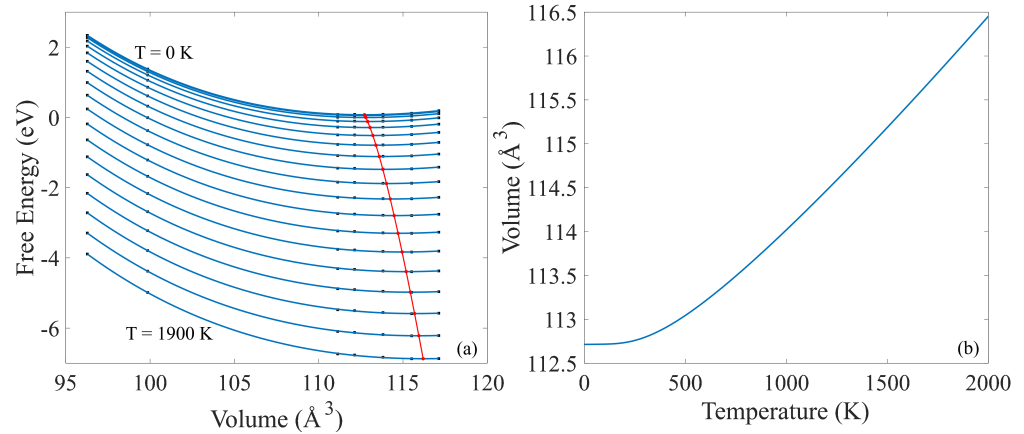


**Figure 4.** (a) Free energy vs. volume of B<sub>4</sub>C at different temperatures, and the equilibrium volume for each temperature shown by the red curve. (b) Volume vs temperature of B<sub>4</sub>C calculated from phonon calculations.

Substituting the  $V(T)$  from Figure 4b in the exponential functions fitted to the static elastic stiffness constants ( $C_{ij}(V)$ ) from Figure 3 results in temperature-dependent elastic stiffness constants ( $C_{ij}(T)$ ). Figure 5 illustrates the six independent elastic constants of the single crystal B<sub>4</sub>C structures at different temperatures. It is evident that at temperatures below 100 K, all elastic constants maintain an almost constant value, attributed to the minimal vibration of atoms at those temperatures. All elastic constants except  $C_{44}$  show a decreasing trend with increasing temperature.  $C_{44}$  exhibits almost no change with temperature, demonstrating the anisotropic behavior of boron carbide. It was observed that all volume-dependent  $C_{ij}$ s excluding  $C_{44}$  exhibit decreasing trends with the volume changes (shown in Figure 3). In contrast,  $C_{44}$  has an increasing trend at volumes lower than the equilibrium volume. After reaching the equilibrium volume, the rate of increase diminishes significantly, resulting in an almost constant value at higher volumes. Since, in the temperature-dependent results, the zero temperature corresponds to the ground state of the material, the effects of structural shrinking at temperatures below zero Kelvin are ignored. Thus, the observed trends in  $C_{ij}(T)$  align closely with those of  $C_{ij}(V)$  at volumes higher than the equilibrium volume.

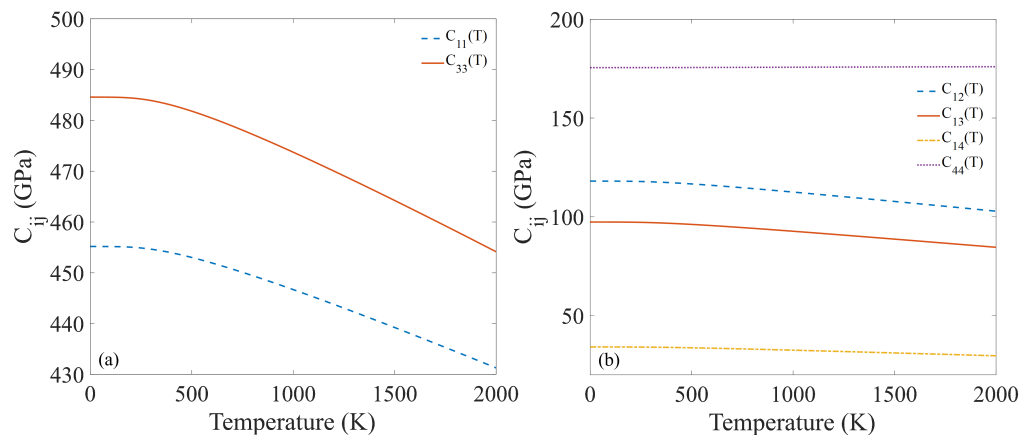


**Figure 5.** Temperature-dependent 6 independent elastic constants of B<sub>4</sub>C (a)  $C_{11}$  and  $C_{33}$  and (b)  $C_{12}$ ,  $C_{13}$ ,  $C_{14}$ , and  $C_{44}$ .

### 3.4. Temperature-Dependent Thermal Expansion Coefficient and Bulk Modulus

The temperature-dependent thermal expansion coefficient (TEC) of boron carbide is also predicted from the quasi-harmonic approach. As a result of strong covalent bonds between B and C atoms in boron carbide, its thermal expansion coefficient is measured to be much lower compared to other materials such as metals and polymers (e.g., zinc:  $30 \times 10^{-6}$  [77], aluminum:  $23 \times 10^{-6}$  [77], and polyethylene:  $100 \times 10^{-6}$  [78] at room temperature). Figure 6a shows the anticipated temperature-dependent TEC of B<sub>4</sub>C boron carbide alongside existing literature data [26,79–82]. Most of the available data are from experiments performed at room temperature (298 K). For example, Tsagareishvili [80], Hollenberg [82], and Telle [81] measured the TEC for boron carbide at room temperature as  $5.73 \times 10^{-6}$ ,  $8.00 \times 10^{-6}$ , and  $9.50 \times 10^{-6}$  respectively. The calculated TEC in this study at room temperature is predicted to be  $7.54 \times 10^{-6}$ , a value consistent with the established range of previously recorded data. At elevated temperatures, the extent of the established data is significantly reduced, and the available data are often derived from experiments conducted on the polycrystalline structures of boron carbide, typically exhibiting defects [26]. The presence of defects such as vacancies, impurities, and point defects can distort the regular arrangement of atoms and lattice symmetry, contributing to a different TEC [83]. Moreover, the grain boundaries and various crystallographic orientations in polycrystalline structures result in an overall expansion that may be lower than that of a perfect single crystal [83]. Kuliiev et al. [26] predicted that the TEC of B<sub>4</sub>C within the temperature range 298–1273 K follows an almost linear trend with an average of  $6 \times 10^{-6}$ . Thevenot [79] used the following equation to determine the TEC of boron carbide:  $\alpha = 3.016 \times 10^{-6} + 4.30 \times 10^{-9}T - 9.18 \times 10^{-13}T^2$  ( $T$  in °C). However, in the two previous temperature-dependent studies, the TEC at room temperature was lower than the established range, resulting in an overall lower TEC at elevated temperatures compared to the case of the perfect single crystal B<sub>4</sub>C studied here.

Additionally, a comparison between the TEC of advanced ceramics, including boron carbide (B<sub>4</sub>C), alumina (Al<sub>2</sub>O<sub>3</sub>) [34], and silicon carbide (SiC) [84] along with the room temperature experimental results [85,86] of them are illustrated in Figure 6b to capture the trends in TEC for these materials. It is evident that these materials exhibit a similar pattern, characterized by a very low to negligible increase in TEC at temperatures below 100 K, followed by a sharp rise until approximately 500–700 K, and then a gradual increase until it approaches a nearly constant value. This trend is attributed to the transition from internal energy dominance to vibrational entropy dominance, indicating significant changes in the material's behavior as temperature increases. At low temperatures (<100 K), the atomic vibrations and motions are minimal leading to less expansion when subjected to a temperature change [47,50]. As the temperature rises to an intermediate range, the vibrational motion of atoms becomes more prominent resulting in a more rapid expansion. As the temperature increases, reaching an elevated range (e.g., near melting point), the material may undergo phase transitions that affect its thermal expansion behavior [47]. At these higher temperatures, the TEC still increases, but the rate of increase tends to be more gradual. The material may approach a nearly constant value as it reaches a state where further increases in temperature have a diminishing impact on the expansion behavior.

As the final result, the temperature-dependent bulk modulus of boron carbide is presented in Figure 7. Similar to the TEC results, most of the available data are from experiments and modeling performed at room temperature rather than elevated temperatures. Previously performed experiments at room temperature resulted in the following data: 246 GPa by Dekura et al. [72], 235 GPa by Manghnani et al. [29], and 237 GPa by Dodd et al. [27]. Moreover, the bulk modulus was predicted as 221 GPa by Taylor et al. [28] and 298 GPa by Aydin et al. [32]. The first-principles calculation produced in this present study with the phonon model resulted in 228 GPa at room temperature, which is in alignment with the data from the literature. In the same experiment that Kuliiev et al. [26] obtained TEC, they also provided the bulk modulus at higher temperatures. The results from our study follow the same decreasing trend of their work and the highest error value

is equal to 9%. This error, along with the variations in trends, can be attributed to differences in the studied structure. The experimental studies use polycrystals with defects, whereas our investigation focuses on a perfect single crystal structure. Similar to the elastic constants, the bulk modulus exhibits negligible changes at temperatures below 100 K.

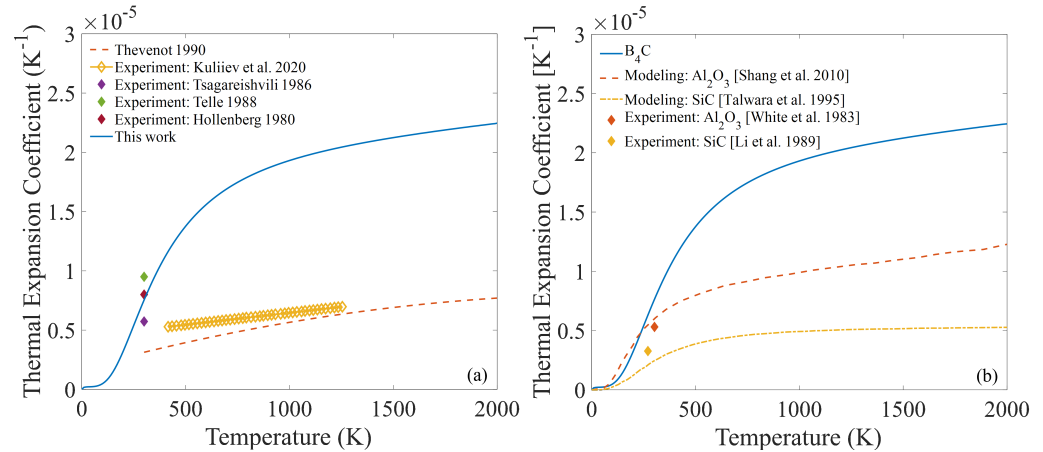


**Figure 6.** Temperature-dependent thermal expansion coefficient of (a)  $\text{B}_4\text{C}$  alongside the literature data [26,79–82] and (b) comparison between TEC of advanced ceramics alongside their room temperature modeling [34,84] and experimental data [85,86].

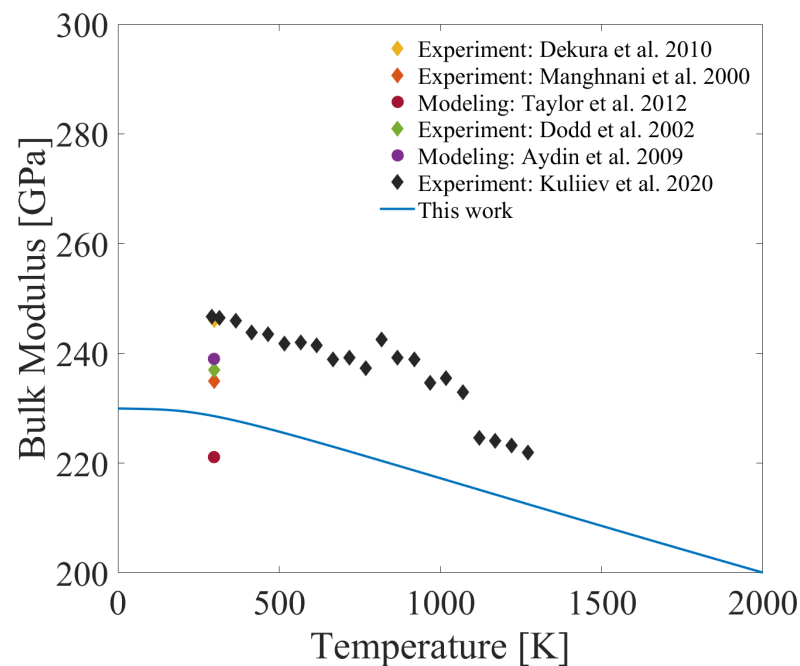


**Figure 7.** Temperature-dependent bulk modulus of  $\text{B}_4\text{C}$  alongside the bulk modulus obtained from other experiments [26,27,29,72] and modeling works [28,32].

### 3.5. Limitations

A potential limitation of this work is the use of the quasi-harmonic approximation, which incorporates the volume dependence of phonon frequencies as a component of anharmonic effects. In the quasi-harmonic approximation, phonon–phonon coupling is neglected, leading to limitations, particularly near the melting temperature where this coupling becomes significant [47]. Another potential limitation of this study was the exclusive consideration of the  $\text{B}_4\text{C}$  configuration of boron carbide. The small difference between the atomic number of  $^{10}\text{B}$  and  $^{12}\text{C}$  makes the precise composition and distribution of carbon atoms difficult to measure [79]. In addition, this chemical similarity induces substitutional

disorder, causing changes in the local atomic arrangement and carbon concentration in boron carbide. The substitution of the central carbon in the CCC chain with the boron in the polar site of the icosahedra results in a more thermodynamically stable structure with a lower energy with a configuration of  $C_{11}C_pCBC$  [87–89]. These variations in boron carbide configurations and chain arrangements lead to different mechanical behavior and stabilities in structures [28,90]. Exploring various stoichiometries in boron carbide provides opportunities for future investigations to further refine our comprehension of this material in extreme environments.

#### 4. Conclusions

In conclusion, this study investigates the temperature-dependent elastic and thermal properties of rhombohedral  $B_4C$  boron carbide, revealing its intricate mechanical response and thermal behavior. Using a quasi-harmonic approach involving static DFT simulations and first-principles phonon calculations, the exploration of elastic constants, thermal properties (Helmholtz free energy, entropy, and heat capacity), and thermal expansion coefficient (TEC) versus temperature provided valuable insights into the material's stability and performance at elevated temperatures. The comprehensive validation of our first-principles calculations against structural parameters and E-V fitting with mBM EOS establishes the reliability of our findings. Moreover, the comparison of TEC with other advanced ceramics demonstrates similar trends emphasizing the influence of atomic structure on material properties. Given the unexplored behavior of single crystal boron carbide at elevated temperatures, the obtained TEC ( $7.54 \times 10^{-6} \text{ K}^{-1}$ ) and bulk modulus (228 GPa) from the quasi-harmonic approach were compared with the room temperature results from literature experiments [27,29,72,80–82] and models [28,31,32]. This comparison showed that the predicted results aligned closely with literature data (TEC =  $5.73\text{--}9.50 \times 10^{-6} \text{ K}^{-1}$ ,  $B = 221\text{--}246 \text{ GPa}$ ). This work presents the variation in elastic stiffness constants, average thermal expansion coefficient, and bulk modulus of single crystal  $B_4C$  across a broad temperature range from 0 to 2000 K. Overall, this work advances our fundamental understanding of boron carbide at elevated temperatures and provides crucial information for optimizing its design across various extreme environment applications, including satellite and aerospace components [6,12], as well as radiation shielding [10,91].

**Supplementary Materials:** The following supporting information can be downloaded at: <https://www.mdpi.com/article/10.3390/ceramics7010015/s1> Figure S1: Temperature-dependent thermodynamic properties of  $B_4C$  for different volumes. (a) Helmholtz free energy, (b) entropy, and (c) heat capacity at constant volume.

**Author Contributions:** Conceptualization, S.S., W.S. and J.D.H.; methodology, S.S.; software, S.S.; validation, S.S., W.S. and J.D.H.; formal analysis, S.S.; investigation, S.S.; resources, W.S. and J.D.H.; writing—original draft preparation, S.S.; writing—review and editing, W.S. and J.D.H.; visualization, S.S.; supervision, W.S. and J.D.H.; project administration, W.S. and J.D.H.; funding acquisition, J.D.H. All authors have read and agreed to the published version of the manuscript.

**Funding:** This work is supported by the Natural Sciences and Engineering Research Council of Canada Discovery Grant (Grant #2023-04457), and contributions from the George Ford Chair in Materials Engineering to JDH.

**Data Availability Statement:** Data will be made available on request.

**Acknowledgments:** This research was enabled in part by support provided by the Digital Research Alliance of Canada ([www.alliancecan.ca](http://www.alliancecan.ca) (accessed on 13 December 2023)) via Cedar cluster.

**Conflicts of Interest:** The authors declare no conflicts of interest.

## Abbreviations

The following abbreviations are used in this manuscript:

DFT	Density Functional Theory
TEC	Thermal Expansion Coefficient
MD	Molecular Dynamics
EOS	Equation of State
BM	Birch–Murnaghan
mBM	Modified Birch–Murnaghan
DOS	Density of States
VASP	Vienna Ab Initio Simulation Package
GGA	Generalized Gradient Approximation
SCF	Self-Consistent Field

## References

1. Roy, T.; Subramanian, C.; Suri, A. Pressureless sintering of boron carbide. *Ceram. Int.* **2006**, *32*, 227–233. [[CrossRef](#)]
2. Swab, J.J.; Meredith, C.S.; Casem, D.T.; Gamble, W.R. Static and dynamic compression strength of hot-pressed boron carbide using a dumbbell-shaped specimen. *J. Mater. Sci.* **2017**, *52*, 10073–10084. [[CrossRef](#)]
3. Vargas-Gonzalez, L.; Speyer, R.F.; Campbell, J. Flexural strength, fracture toughness, and hardness of silicon carbide and boron carbide armor ceramics. *Int. J. Appl. Ceram. Technol.* **2010**, *7*, 643–651. [[CrossRef](#)]
4. Werheit, H.; Leithe-Jasper, A.; Tanaka, T.; Rotter, H.; Schwetz, K. Some properties of single-crystal boron carbide. *J. Solid State Chem.* **2004**, *177*, 575–579. [[CrossRef](#)]
5. Matkovich, V.I.; Samsonov, G.V.; Hagenmuller, P. *Boron and Refractory Borides*; Springer: Berlin/Heidelberg, Germany, 1977.
6. Varshney, V. Molecular dynamics methodologies for predicting thermal transport in aerospace polymers and their composites. In *Hybrid Atomic-Scale Interface Design for Materials Functionality*; Elsevier: Amsterdam, The Netherlands, 2021; pp. 19–34.
7. El Messiry, M. *Protective Armor Engineering Design*; Apple Academic Press: Palm Bay, FL, USA, 2019.
8. Turatti, A.M.; Pereira, A.S. Wear resistant boron carbide compacts produced by pressureless sintering. *Ceram. Int.* **2017**, *43*, 7970–7977. [[CrossRef](#)]
9. Domnich, V.; Reynaud, S.; Haber, R.A.; Chhowalla, M. Boron carbide: Structure, properties, and stability under stress. *J. Am. Ceram. Soc.* **2011**, *94*, 3605–3628. [[CrossRef](#)]
10. Sariyer, D.; Küçer, R.; Küçer, N. Neutron shielding properties of concretes containing boron carbide and ferro-boron. *Procedia-Soc. Behav. Sci.* **2015**, *195*, 1752–1756. [[CrossRef](#)]
11. Chevalier, J.; Gremillard, L. Ceramics for medical applications: A picture for the next 20 years. *J. Eur. Ceram. Soc.* **2009**, *29*, 1245–1255. [[CrossRef](#)]
12. Levchenko, I.; Bazaka, K.; Belmonte, T.; Keidar, M.; Xu, S. Advanced Materials for Next-Generation Spacecraft. *Adv. Mater.* **2018**, *30*, 1802201. [[CrossRef](#)]
13. Goldman, N. *Computational Approaches for Chemistry under Extreme Conditions*; Springer: Berlin/Heidelberg, Germany, 2019; Volume 28.
14. Mishin, Y. Machine-learning interatomic potentials for materials science. *Acta Mater.* **2021**, *214*, 116980. [[CrossRef](#)]
15. Suri, A.; Subramanian, C.; Sonber, J.; Murthy, T.C. Synthesis and consolidation of boron carbide: A review. *Int. Mater. Rev.* **2010**, *55*, 4–40. [[CrossRef](#)]
16. Konovalikhin, S.; Ponomarev, V. Carbon in boron carbide: The crystal structure of B11.4C3.6. *Russ. J. Inorg. Chem.* **2009**, *54*, 197–203. [[CrossRef](#)]
17. Morawiec, A. Review of deterministic methods of calculation of polycrystal elastic constants. *Textures Microstruct.* **1994**, *22*, 139–167. [[CrossRef](#)]
18. Fahrenholtz, W.G.; Hilmas, G.E. Ultra-high temperature ceramics: Materials for extreme environments. *Scr. Mater.* **2017**, *129*, 94–99. [[CrossRef](#)]
19. Saha, D.; Ghara, D.K.; Pal, M. Nanoporous  $\gamma$ -alumina based novel sensor to detect trace moisture in high temperature and high pressure environment. *Sens. Actuators B Chem.* **2016**, *222*, 1043–1049. [[CrossRef](#)]
20. Medvedovski, E. Influence of corrosion and mechanical loads on advanced ceramic components. *Ceram. Int.* **2013**, *39*, 2723–2741. [[CrossRef](#)]
21. Chang, J.; Chen, Z.; Hogan, J.D. Molecular Dynamics Simulations Correlating Mechanical Property Changes of Alumina with Atomic Voids under Triaxial Tension Loading. *Modelling* **2023**, *4*, 211–223. [[CrossRef](#)]
22. Yang, A.; Romanyk, D.; Hogan, J.D. High-velocity impact study of an advanced ceramic using finite element model coupling with a machine learning approach. *Ceram. Int.* **2023**, *49*, 10481–10498. [[CrossRef](#)]
23. Parsazadeh, M.; Fisher, G.; McDonald, A.; Hogan, J.D. Computational modelling of the effect of microstructure on the abrasive wear resistance of tungsten-carbide nickel composite coatings under sub-critical cyclic impact loading. *Ceram. Int.* **2022**, *48*, 14338–14348. [[CrossRef](#)]

24. Manafi Farid, H.; McDonald, A.; Hogan, J.D. Impact Deposition Behavior of Al/B<sub>4</sub>C Cold-Sprayed Composite Coatings: Understanding the Role of Porosity on Particle Retention. *Materials* **2023**, *16*, 2525. [[CrossRef](#)]
25. Gogotsi, G.; Groushevsky, Y.L.; Dashevskaya, O.; Gogotsi, Y.G.; Lavrenko, V. Complex investigation of hot-pressed boron carbide. *J. Less Common Met.* **1986**, *117*, 225–230. [[CrossRef](#)]
26. Kulliev, R.; Orlovskaya, N.; Hyer, H.; Sohn, Y.; Lugovy, M.; Ha, D.; Radovic, M.; Castle, E.G.; Reece, M.J.; Vallachira Warriam Sasikumar, P.; et al. Spark Plasma Sintered B<sub>4</sub>C—Structural, Thermal, Electrical and Mechanical Properties. *Materials* **2020**, *13*, 1612. [[CrossRef](#)]
27. Dodd, S.; Saunders, G.; James, B. Temperature and pressure dependences of the elastic properties of ceramic boron carbide (B<sub>4</sub>C). *J. Mater. Sci.* **2002**, *37*, 2731–2736. [[CrossRef](#)]
28. Taylor, D.E.; McCauley, J.W.; Wright, T. The effects of stoichiometry on the mechanical properties of icosahedral boron carbide under loading. *J. Phys. Condens. Matter* **2012**, *24*, 505402. [[CrossRef](#)] [[PubMed](#)]
29. Manghnani, M.H.; Wang, Y.; Li, F.; Zinin, P.; Rafaniello, W. Elastic and vibrational properties of B<sub>4</sub>C to 21 GPa. *Sci. Technol. High Press.* **2000**, *2*, 25–30.
30. Gieske, J.; Aselage, T.; Emin, D. Elastic properties of boron carbides. In *AIP Conference Proceedings*; American Institute of Physics: College Park, MD, USA, 1991; Volume 231, pp. 376–379.
31. Lee, S.; Bylander, D.; Kleinman, L. Elastic moduli of B<sub>12</sub> and its compounds. *Phys. Rev. B* **1992**, *45*, 3245. [[CrossRef](#)] [[PubMed](#)]
32. Aydin, S.; Simsek, M. Hypothetically superhard boron carbide structures with a B<sub>11</sub>C icosahedron and three-atom chain. *Phys. Status Solidi (B)* **2009**, *246*, 62–70. [[CrossRef](#)]
33. Farbaniec, L.; Hogan, J.; McCauley, J.; Ramesh, K. Anisotropy of mechanical properties in a hot-pressed boron carbide. *Int. J. Appl. Ceram. Technol.* **2016**, *13*, 1008–1016. [[CrossRef](#)]
34. Shang, S.L.; Zhang, H.; Wang, Y.; Liu, Z.K. Temperature-dependent elastic stiffness constants of  $\alpha$ - and  $\theta$ -Al<sub>2</sub>O<sub>3</sub> from first-principles calculations. *J. Phys. Condens. Matter* **2010**, *22*, 375403. [[CrossRef](#)] [[PubMed](#)]
35. Shang, S.L.; Wang, Y.; Kim, D.; Liu, Z.K. First-principles thermodynamics from phonon and Debye model: Application to Ni and Ni<sub>3</sub>Al. *Comput. Mater. Sci.* **2010**, *47*, 1040–1048. [[CrossRef](#)]
36. Tang, B.; He, Y.; Goddard III, W.A.; An, Q. First principles predicting enhanced ductility of boride carbide through magnesium microalloying. *J. Am. Ceram. Soc.* **2019**, *102*, 5514–5523. [[CrossRef](#)]
37. Shen, Y.; Reddy, K.M.; Li, J.; Chen, M.; An, Q. Atomistic origin of shear induced quasi-plastic deformation in boron carbide. *Acta Mater.* **2023**, *249*, 118828. [[CrossRef](#)]
38. Kocer, E.; Ko, T.W.; Behler, J. Neural Network Potentials: A Concise Overview of Methods. *Annu. Rev. Phys. Chem.* **2022**, *73*. [[CrossRef](#)]
39. Zuo, Y.; Chen, C.; Li, X.; Deng, Z.; Chen, Y.; Behler, J.; Csányi, G.; Shapeev, A.V.; Thompson, A.P.; Wood, M.A.; et al. Performance and cost assessment of machine learning interatomic potentials. *J. Phys. Chem. A* **2020**, *124*, 731–745. [[CrossRef](#)]
40. Shang, S.; Wang, Y.; Liu, Z.K. First-principles calculations of phonon and thermodynamic properties in the boron-alkaline earth metal binary systems: B-Ca, B-Sr, and B-Ba. *Phys. Rev. B* **2007**, *75*, 024302. [[CrossRef](#)]
41. Rou, S.; Chandran, K.R. First principles calculation of single-crystal elastic constants of titanium tetraboride (Ti<sub>3</sub>B<sub>4</sub>) and experimental validation. *J. Am. Ceram. Soc.* **2018**, *101*, 4308–4320. [[CrossRef](#)]
42. Nikolussi, M.; Shang, S.; Gressmann, T.; Leineweber, A.; Mittemeijer, E.; Wang, Y.; Liu, Z.K. Extreme elastic anisotropy of cementite, Fe<sub>3</sub>C: First-principles calculations and experimental evidence. *Scr. Mater.* **2008**, *59*, 814–817. [[CrossRef](#)]
43. Cheng, C.; Reddy, K.M.; Hirata, A.; Fujita, T.; Chen, M. Structure and mechanical properties of boron-rich boron carbides. *J. Eur. Ceram. Soc.* **2017**, *37*, 4514–4523. [[CrossRef](#)]
44. DeVries, M.; Subhash, G.; Awasthi, A. Shocked ceramics melt: An atomistic analysis of thermodynamic behavior of boron carbide. *Phys. Rev. B* **2020**, *101*, 144107. [[CrossRef](#)]
45. Pillai, H.G.; Madam, A.K.; Chandra, S.; Cheruvalath, V.M. Semiconducting B<sub>13</sub>C<sub>2</sub> system: Structure search and DFT-based analysis. *Mater. Res. Express* **2019**, *6*, 046544. [[CrossRef](#)]
46. Li, L.; Weidner, D.J.; Brodholt, J.; Alfe, D.; Price, G.D.; Caracas, R.; Wentzcovitch, R. Elasticity of CaSiO<sub>3</sub> perovskite at high pressure and high temperature. *Phys. Earth Planet. Inter.* **2006**, *155*, 249–259. [[CrossRef](#)]
47. Ritz, E.T.; Li, S.J.; Benedek, N.A. Thermal expansion in insulating solids from first principles. *J. Appl. Phys.* **2019**, *126*, 171102. [[CrossRef](#)]
48. Eschrig, H. *The Fundamentals of Density Functional Theory*; Springer: Berlin/Heidelberg, Germany, 1996; Volume 32.
49. McGaughey, A.J.; Jain, A.; Kim, H.Y.; Fu, B. Phonon properties and thermal conductivity from first principles, lattice dynamics, and the Boltzmann transport equation. *J. Appl. Phys.* **2019**, *125*, 011101. [[CrossRef](#)]
50. Born, M.; Huang, K. *Dynamical Theory of Crystal Lattices*; Oxford University Press: Oxford, UK, 1996.
51. Fultz, B. Vibrational thermodynamics of materials. *Prog. Mater. Sci.* **2010**, *55*, 247–352. [[CrossRef](#)]
52. Wang, Y.; Liu, Z.K.; Chen, L.Q. Thermodynamic properties of Al, Ni, NiAl, and Ni<sub>3</sub>Al from first-principles calculations. *Acta Mater.* **2004**, *52*, 2665–2671. [[CrossRef](#)]
53. Wang, D.Y.; Yan, Q.; Wang, B.; Wang, Y.X.; Yang, J.; Yang, G. Predicted boron-carbide compounds: A first-principles study. *J. Chem. Phys.* **2014**, *140*, 224704. [[CrossRef](#)] [[PubMed](#)]
54. Birch, F. Finite strain isotherm and velocities for single-crystal and polycrystalline NaCl at high pressures and 300 K. *J. Geophys. Res. Solid Earth* **1978**, *83*, 1257–1268. [[CrossRef](#)]

55. Teter, D.; Gibbs, G.V.; Boisen, M.B., Jr.; Allan, D.; Teter, M. First-principles study of several hypothetical silica framework structures. *Phys. Rev. B* **1995**, *52*, 8064. [CrossRef]
56. Togo, A. First-principles phonon calculations with phonopy and phono3py. *J. Phys. Soc. Jpn.* **2023**, *92*, 012001. [CrossRef]
57. Kresse, G.; Hafner, J. Ab initio molecular dynamics for liquid metals. *Phys. Rev. B* **1993**, *47*, 558. [CrossRef]
58. Kresse, G.; Furthmüller, J. Efficient iterative schemes for ab initio total-energy calculations using a plane-wave basis set. *Phys. Rev. B* **1996**, *54*, 11169. [CrossRef]
59. Perdew, J.P.; Burke, K.; Ernzerhof, M. Generalized gradient approximation made simple. *Phys. Rev. Lett.* **1996**, *77*, 3865. [CrossRef]
60. Blöchl, P.E.; Jepsen, O.; Andersen, O.K. Improved tetrahedron method for Brillouin-zone integrations. *Phys. Rev. B* **1994**, *49*, 16223. [CrossRef]
61. Heywang, W.; Zaininger, K. Silicon: The semiconductor material. In *Silicon: Evolution and Future of a Technology*; Springer: Berlin/Heidelberg, Germany, 2004; pp. 25–42.
62. Nekrashevich, S.; Gritsenko, V. Electronic structure of silicon dioxide (a review). *Phys. Solid State* **2014**, *56*, 207–222. [CrossRef]
63. Hushur, A.; Manghnani, M.H.; Werheit, H.; Dera, P.; Williams, Q. High-pressure phase transition makes B4. 3C boron carbide a wide-gap semiconductor. *J. Phys. Condens. Matter* **2016**, *28*, 045403. [CrossRef] [PubMed]
64. Brown-Shaklee, H.J.; Neuman, E.W.; Fahrenholtz, W.G.; Hilmas, G.E. Optical characterization of boron carbide powders synthesized with varying B-to-C ratios. *J. Am. Ceram. Soc.* **2023**, *106*, 1932–1944. [CrossRef]
65. Kresse, G.; Joubert, D. From ultrasoft pseudopotentials to the projector augmented-wave method. *Phys. Rev. B* **1999**, *59*, 1758. [CrossRef]
66. Pulay, P. Convergence acceleration of iterative sequences. The case of SCF iteration. *Chem. Phys. Lett.* **1980**, *73*, 393–398. [CrossRef]
67. Wang, V.; Xu, N.; Liu, J.C.; Tang, G.; Geng, W.T. VASPKIT: A user-friendly interface facilitating high-throughput computing and analysis using VASP code. *Comput. Phys. Commun.* **2021**, *267*, 108033. [CrossRef]
68. Togo, A.; Chaput, L.; Tadano, T.; Tanaka, I. Implementation strategies in phonopy and phono3py. *J. Phys. Condens. Matter* **2023**, *35*, 353001. [CrossRef]
69. Momma, K.; Izumi, F. VESTA 3 for three-dimensional visualization of crystal, volumetric and morphology data. *J. Appl. Crystallogr.* **2011**, *44*, 1272–1276. [CrossRef]
70. Kwei, G.H.; Morosin, B. Structures of the boron-rich boron carbides from neutron powder diffraction: Implications for the nature of the inter-icosahedral chains. *J. Phys. Chem.* **1996**, *100*, 8031–8039. [CrossRef]
71. McClellan, K.; Chu, F.; Roper, J.; Shindo, I. Room temperature single crystal elastic constants of boron carbide. *J. Mater. Sci.* **2001**, *36*, 3403–3407. [CrossRef]
72. Dekura, H.; Shirai, K.; Yanase, A. Metallicity of boron carbides at high pressure. In *Journal of Physics: Conference Series*; IOP Publishing: Bristol, UK, 2010; Volume 215, p. 012117.
73. Bylander, D.; Kleinman, L.; Lee, S. Self-consistent calculations of the energy bands and bonding properties of B12C3. *Phys. Rev. B* **1990**, *42*, 1394. [CrossRef] [PubMed]
74. Project, T.M. Materials Data on B4C (mp-696746) by Materials Project (v2023.11.1). Available online: <https://next-gen.materialsproject.org/materials/mp-696746> (accessed on 3 December 2023).
75. An, Q.; Goddard III, W.A. Atomistic origin of brittle failure of boron carbide from large-scale reactive dynamics simulations: Suggestions toward improved ductility. *Phys. Rev. Lett.* **2015**, *115*, 105501. [CrossRef] [PubMed]
76. Pavlovskii, M.S.; Andryushin, N. Calculating the Lattice Dynamics in the RFe<sub>3</sub>(BO<sub>3</sub>)<sub>4</sub> Crystals in the Quasi-Harmonic Approximation. *Phys. Solid State* **2019**, *61*, 2019–2025. [CrossRef]
77. Zhang, B.; Li, X.; Li, D. Assessment of thermal expansion coefficient for pure metals. *Calphad* **2013**, *43*, 7–17. [CrossRef]
78. Shen, M.; Hansen, W.N.; Romo, P.C. Thermal expansion of the polyethylene unit cell. *J. Chem. Phys.* **1969**, *51*, 425–430. [CrossRef]
79. Thevenot, F. Boron carbide—a comprehensive review. *J. Eur. Ceram. Soc.* **1990**, *6*, 205–225. [CrossRef]
80. Tsagareishvili, G.; Nakashidze, T.; Jobava, J.S.; Lomidze, G.; Khulelidze, D.; Tsagareishvili, D.S.; Tsagareishvili, O. Thermal expansion of boron and boron carbide. *J. Less Common Met.* **1986**, *117*, 159–161. [CrossRef]
81. Telle, R. Boride—eine neue Hartstoffgeneration? *Chem. Unserer Zeit* **1988**, *22*, 93–99. [CrossRef]
82. Hollenberg, G. Thermally induced stresses and fractures in boron carbide pellets. *Bull. Am. Ceram. Soc.* **1980**, *59*, 538–548.
83. Wang, K.; Reeber, R. Thermal defects and thermal expansion of ionic crystals at high temperatures. *Phys. Status Solidi (A)* **1994**, *146*, 621–627. [CrossRef]
84. Talwar, D.; Sherbondy, J.C. Thermal expansion coefficient of 3C–SiC. *Appl. Phys. Lett.* **1995**, *67*, 3301–3303. [CrossRef]
85. White, G.K.; Roberts, R.B. Thermal expansion of reference materials: Tungsten and  $\alpha$ -Al<sub>2</sub>O<sub>3</sub>. *High Temp.-High Press.* **1983**, *15*, 321–328.
86. Li, Z.; Bradt, R. Thermal expansion and elastic anisotropies of SiC as related to polytype structure. In *Proceedings of the Silicon Carbide'87*, Columbus, OH, USA, 2–5 August 1989.
87. Shirai, K.; Sakuma, K.; Uemura, N. Theoretical study of the structure of boron carbide B<sub>1</sub>3C<sub>2</sub>. *Phys. Rev. B* **2014**, *90*, 064109. [CrossRef]
88. Ektarawong, A.; Simak, S.I.; Alling, B. Structural models of increasing complexity for icosahedral boron carbide with compositions throughout the single-phase region from first principles. *Phys. Rev. B* **2018**, *97*, 174104. [CrossRef]

89. Rasim, K.; Ramlau, R.; Leithe-Jasper, A.; Mori, T.; Burkhardt, U.; Borrmann, H.; Schnelle, W.; Carbogno, C.; Scheffler, M.; Grin, Y. Local atomic arrangements and band structure of boron carbide. *Angew. Chem.* **2018**, *130*, 6238–6243. [[CrossRef](#)]
90. Jay, A.; Hardouin Duparc, O.; Sjakste, J.; Vast, N. Theoretical phase diagram of boron carbide from ambient to high pressure and temperature. *J. Appl. Phys.* **2019**, *125*, 185902. [[CrossRef](#)]
91. Vignesh, S.; JT, W.J.; Nagaveena, S.; Sharma, K.; Khan, A. Boron carbide dispersed epoxy composites for gamma radiation shielding applications. *Vacuum* **2022**, *205*, 111474.

**Disclaimer/Publisher's Note:** The statements, opinions and data contained in all publications are solely those of the individual author(s) and contributor(s) and not of MDPI and/or the editor(s). MDPI and/or the editor(s) disclaim responsibility for any injury to people or property resulting from any ideas, methods, instructions or products referred to in the content.